Direct calculation of thermal emission for three-dimensionally periodic photonic crystal slabs

David L. C. Chan, Marin Soljačić, and J. D. Joannopoulos
Department of Physics and Center for Materials Science and Engineering, Massachusetts Institute of Technology, Cambridge, Massachusetts 02139, USA
(Received 8 May 2006; published 18 September 2006)

We perform direct thermal emission calculations for three-dimensionally periodic photonic crystal slabs using stochastic electrodynamics following the Langevin approach, implemented via a finite-difference time-domain algorithm. We demonstrate that emissivity and absorptivity are equal, by showing that such photonic crystal systems emit as much radiation as they absorb, for every frequency, up to statistical fluctuations. We also study the effect of surface termination on absorption and emission spectra from these systems.

DOI: 10.1103/PhysRevE.74.036615 PACS number(s): 42.70.Qs, 44.40.+a

I. INTRODUCTION

The physics of blackbodies has fascinated and intrigued researchers for well over a century now [1]; properties of their thermal emission provided one of the most important clues for the discovery of quantum mechanics. In practice, most objects have absorption less than that of a blackbody, and are thus referred to as "graybodies." By virtue of Kirchhoff's law, these objects also have subunity emissivity. However, the thermal emission spectra of graybodies can be changed by altering the geometry of the system or the materials used.

Very exciting work has been done recently on three-dimensionally (3D) periodic photonic crystals with photonic band gaps [2–10] concerning enhancement and suppression of thermal emission [3,6,7] and thermophotovoltaic applications [5,8]. Emission and absorption from 2D periodic photonic crystals have been also studied within the contexts of spectral and directional control [11–15], guided resonances [16], thermophotovoltaic generation [17], resonant scattering [18,19], laser action [20], Kirchhoff's law [21,22], coherence [15,23], and spontaneous emission enhancement [13,24,25]. It has been noted that periodic subwavelength scale patterning of metallodielectric systems, i.e., photonic crystals, can modify their thermal emission spectra in many interesting ways [10,12,14,17,22,23,25–28], through various physical effects such as surface plasmons [13,29], resonant-cavity enhancement [30], Bragg reflection [31], and modification of density of states via photonic band gaps [3,5,8,31].

In previous work, most calculations for thermal emission were performed by calculating the absorption and then appealing to Kirchhoff's law, which states that absorptivity and emissivity are equal. This has been shown analytically for a uniform slab. Luo *et al.* [22], following a Langevin approach to stochastic electrodynamics, performed a direct thermal emission calculation for a 2D periodic photonic crystal slab and showed that emissivity was equal to absorptivity (up to thermal fluctuations), thus numerically verifying Kirchhoff's law for such systems.

In this paper, we extend the work done by Luo *et al.* to 3D periodic structures. Using stochastic electrodynamics, we perform direct simulations of emission spectra for 3D periodic structures. We compare these directly calculated emission spectra to the absorption spectra of these systems, and demonstrate that Kirchhoff's law holds for 3D periodic photonic crystal slabs. Moreover, we examine the effect of changing the surface termination of a 3D periodic structure and suggest how it may be used to enhance absorption and emission of a photonic crystal. We also give an in-depth and coherent presentation of the theory of stochastic electrodynamics, including relevant derivations and detailed explanations of our methodology.

This paper is organized as follows: in Sec. II, we describe the theory of stochastic electrodynamics, and how it can be used to perform direct emission calculations. Section III outlines the numerical methods and techniques used in this paper. In Sec. IV, we study a 3D periodic woodpile structure, and show band structure, absorption, and emission calculations. We do the same in Sec. V for a 3D periodic metallodielectric structure. Section VI deals with the effect of surface termination, and how it can be used to enhance emission in these photonic crystal slab structures.

II. THEORY

A. Stochastic electrodynamics and the Langevin approach

Maxwell's equations, as they stand, are classical deterministic field equations. We would like to introduce an element of randomness into these field equations, in order to represent the randomness inherent in thermal fluctuations. We follow the Langevin approach to Brownian motion by introducing a random force term into our equations. There are three ways in which we can proceed: (i) introduce randomness directly in the Newtonian equation of motion, (ii) add a random term to the displacement field, **D**, or (iii) add a random term to the free current density, **J**. These three ways of introducing randomness are entirely equivalent, as we will demonstrate.

The first approach introduces randomness through the addition of a random term in Newton's equation of motion. Modeling charge carriers as damped simple harmonic oscillators driven by an external field **E**, we can write, for a deterministic system, $\ddot{\mathbf{r}}+\gamma\dot{\mathbf{r}}+\omega_0^2\mathbf{r}=e\mathbf{E}/m$, where **r** is the position of the charge carrier, e its charge, m its mass, γ the damping constant of the system, and ω_0 the natural resonant frequency of the system. Converting this to polarization via $\mathbf{P}=ne\mathbf{r}$ (where n is the density of positive charge), we have

$$\frac{d^2\mathbf{P}}{dt^2} + \gamma\frac{d\mathbf{P}}{dt} + \omega_0^2\mathbf{P} = \sigma\mathbf{E}, \tag{1}$$

where $\sigma \equiv ne^2/m$. We introduce a random term ($\mathbf{K}$) to the right-hand side following the Langevin approach:

$$\frac{d^2\mathbf{P}}{dt^2} + \gamma\frac{d\mathbf{P}}{dt} + \omega_0^2\mathbf{P} = \sigma\mathbf{E} + \mathbf{K}(t). \tag{2}$$

Substituting in a harmonic ansatz for $\mathbf{P}$ gives the following solution:

$$\mathbf{P}(\mathbf{r},\omega) = \frac{\sigma\mathbf{E}(\mathbf{r},\omega)}{\omega_0^2 - \omega^2 - i\gamma\omega} + \frac{\mathbf{K}(\mathbf{r},\omega)}{\omega_0^2 - \omega^2 - i\gamma\omega}.$$

Polarization is related to the displacement field via $\mathbf{D}=\mathbf{E}+4\pi\mathbf{P}$. Thus, we see that $\mathbf{D}$ consists of an external field $\mathbf{E}$, the usual nonstochastic polarization-induced component $4\pi\sigma\mathbf{E}(\mathbf{r},\omega)/(\omega_0^2-\omega^2-i\gamma\omega)$, and a random component which we define as

$$\mathbf{Q}(\mathbf{r},\omega) \equiv \frac{4\pi\mathbf{K}(\mathbf{r},\omega)}{\omega_0^2 - \omega^2 - i\gamma\omega}. \tag{3}$$

Thus, a fluctuating polarization ($\mathbf{K}$) in the Newtonian equation of motion is equivalent to a random, fluctuating term ($\mathbf{Q}$) in the displacement field. The fourth Maxwell equation now becomes

$$\nabla \times \mathbf{H} = \frac{4\pi}{c}\mathbf{J} + \frac{1}{c}\frac{\partial}{\partial t}(\mathbf{D} + \mathbf{Q}).$$

Alternatively, instead of introducing randomness to the displacement field, we could just as easily have added a random term $\mathbf{J}_{\text{fluc}}=(1/4\pi)(\partial\mathbf{Q}/\partial t)$ to the free current density $\mathbf{J}$, and the end result would have been the same. Therefore, we have shown that approaches (i), (ii), and (iii) for introducing randomness into Maxwell's equations are entirely equivalent.

B. Statistical properties of thermal fluctuations

Let us proceed with the fluctuating displacement field. The correlation function for $\mathbf{Q}$ has to satisfy a fluctuation-dissipation relation, derived by Rytov [32]:

$$\langle Q_i(\mathbf{r},\omega)Q_j^*(\mathbf{r}',\omega')\rangle = \frac{16\pi^3c^2\,\mathrm{Im}[\epsilon(\omega)]}{\omega^3} \times I_0(\omega,T)\delta_{ij}\delta_{\omega\omega'}\delta(\mathbf{r}-\mathbf{r}'), \tag{4}$$

where Q_i for $i=1,2,3$ are the components of $\mathbf{Q}$, $\langle\cdots\rangle$ denotes ensemble averaging, c is the speed of light, $\mathrm{Im}[\epsilon(\omega)]$ is the imaginary part of the permittivity including the polarization response in the absence of fluctuations [cf. Eq. (1)], and $I_0(\omega,T)=(c/4\pi)D(\omega)E(\omega,T)$. In this expression, $D(\omega)=\omega^2/\pi^2c^3$ is the free-space density of photon states and $E(\omega,T)=\hbar\omega/[\exp(\hbar\omega/kT)-1]$ is the Bose-Einstein energy distribution function at absolute temperature T.

We can also calculate the correlation function for $\mathbf{Q}$ directly from Eq. (3):

$$\langle Q_i(\mathbf{r},\omega)Q_j^*(\mathbf{r}',\omega')\rangle = \frac{(4\pi)^2}{[(\omega_0^2-\omega^2)-i\gamma\omega][(\omega_0^2-\omega'^2)+i\gamma\omega']} \times\langle K_i(\mathbf{r},\omega)K_j^*(\mathbf{r}',\omega')\rangle. \tag{5}$$

The two expressions for the $\mathbf{Q}$ correlation function must be equal. By equating Eqs. (4) and (5), we can learn something about the correlation function of $\mathbf{K}$.

Our first step is to find the imaginary part of the dielectric function. In the absence of fluctuations, the dielectric function for our system is

$$\epsilon(\omega) = 1 + 4\pi\frac{|\mathbf{P}|}{|\mathbf{E}|} = 1 + \frac{4\pi\sigma}{\omega_0^2 - \omega^2 - i\gamma\omega}.$$

Therefore, the imaginary part is

$$\mathrm{Im}[\epsilon(\omega)] = \frac{4\pi\sigma\gamma\omega}{(\omega_0^2-\omega^2)^2 + \gamma^2\omega^2}. \tag{6}$$

Combining Eqs. (4)–(6), gives

$$\langle K_i(\mathbf{r},\omega)K_j^*(\mathbf{r}',\omega')\rangle = \frac{4\pi^2c^2\sigma\gamma}{\omega^2}I_0(\omega,T)\delta_{ij}\delta_{\omega\omega'}\delta(\mathbf{r}-\mathbf{r}'). \tag{7}$$

This expression for the $\mathbf{K}$ correlation function gives us information about the distribution of the Langevin noise term. However, since finite difference numerical simulations require the discretization of space, for our calculations, it will be necessary to convert the Dirac delta function in $\mathbf{r}$ to a Kronecker delta.

The delta function $\delta(\mathbf{r}-\mathbf{r}')$ can be defined as follows:

$$f(\mathbf{r}) = \int_V f(\mathbf{r}')\delta(\mathbf{r}-\mathbf{r}')d^3\mathbf{r}'$$

for any function $f(\mathbf{r})$ over some volume V. We can discretize the above definition by approximating the integral by a discrete summation:

$$f(\mathbf{r}) = \sum_V f(\mathbf{r}')\frac{\delta_{\mathbf{r}\mathbf{r}'}}{\Delta V}\Delta V,$$

where ΔV is the volume element used in the simulation. Therefore, we can go from the continuous to the discrete limit by making the replacement $\delta(\mathbf{r}-\mathbf{r}')\to\delta_{\mathbf{r}\mathbf{r}'}/\Delta V$. Making this substitution in Eq. (7) gives us the discretized version (where we have set $\mathbf{r}'=\mathbf{r}$):

$$\langle K_i(\mathbf{r},\omega)K_j^*(\mathbf{r},\omega')\rangle = \frac{4\pi^2\sigma\gamma\delta_{ij}\delta_{\omega\omega'}}{\Delta V}\frac{I_0(\omega,T)}{(\omega/c)^2}. \tag{8}$$

Note that in the high temperature limit, where $\hbar\omega \ll kT$, the Bose-Einstein energy density function $\hbar\omega/[\exp(\hbar\omega/kT)-1]\approx kT$, and so $I_0(\omega,T)\sim\omega^2$. This exactly cancels out the frequency dependence on the right-hand side of Eq. (8), leading to a white-noise spectrum in $\mathbf{K}$. However, we will find in the next section that emissivity can be simulated by a white-noise spectrum for *all* frequencies.

C. Calculation of emissivity

To calculate emissivity, the target thermal emission intensity needs to be normalized by that of the free-space Planck radiation. The linearity of the system ensures that this normalization procedure amounts to dividing the right-hand side of Eq. (8) by the blackbody radiation collected within an element of a solid angle. It can be shown that [33] the Planck radiation emitted into an element of solid angle $d\Omega$ is $I_0(\omega,T)\cos\theta\, d\Omega$.

However, in finite-difference time-domain calculations of photonic crystal systems implementing Bloch-periodic boundary conditions in the xz and yz faces, directions are specified using wave vectors k_x and k_y instead of polar and azimuthal angles θ and ϕ. Thus, the calculable quantity is $\langle K_i(\mathbf{r},\omega)K_j'^*(\mathbf{r},\omega')\rangle dk_x dk_y$ for emission into a wave vector range (k_x,k_x+dk_x) and (k_y,k_y+dk_y). It is straightforward to calculate the Jacobian to convert from angles to wave vector components: $dk_x dk_y=(\omega/c)^2\sin\theta\cos\theta d\theta\, d\phi=(\omega/c)^2\cos\theta\, d\Omega$. The Planck intensity of emission into $d\Omega$ is therefore

$$I_0(\omega,T)\cos\theta d\Omega = I_0(\omega,T)\frac{dk_x dk_y}{(\omega/c)^2}. \tag{9}$$

Thus, the normalization factor is $I_0(\omega,T)/(\omega/c)^2$. Dividing Eq. (8) by this factor gives the emissivity spectrum for a given (k_x,k_y):

$$\langle K_i'(\mathbf{r},\omega)K_j'^*(\mathbf{r},\omega')\rangle = \frac{4\pi^2 C'^2\sigma\gamma\delta_{ij}\delta_{\omega\omega'}}{\Delta V}, \tag{10}$$

where $\mathbf{K}'(\mathbf{r},\omega)\equiv C'\mathbf{K}(\mathbf{r},\omega)\sqrt{(\omega/c)^2/I_0(\omega,T)}$, and we are considering emission into an element of a wave vector specified by $dk_x dk_y$. C' is a dimension-correcting factor that depends only on the discretization details of the system. It converts a fluctuation in polarization to a fluctuation in emissivity. Fourier-transforming back to the time domain gives

$$\begin{aligned}\langle K_i'(\mathbf{r},t)K_j'^*(\mathbf{r},t')\rangle &= \frac{1}{N^2}\sum_{\omega\omega'}\langle K_i'(\mathbf{r},\omega)K_j'^*(\mathbf{r},\omega')e^{-i\omega t+i\omega' t'}\rangle \\ &= \frac{4\pi^2 C'^2}{N\Delta V}\sigma\gamma\delta_{ij}\delta_{tt'}\end{aligned} \tag{11}$$

with N being the number of time steps used in the Fourier transform. Thus, we can simulate emissivity by producing a time series of random drawings from a distribution with variance $\langle|K_i'(\mathbf{r},t)|^2\rangle$. Since this is the only physical constraint on the distribution of $\mathbf{K}$, we are free to choose a simple and tractable distribution for our simulations. We choose a uniform distribution:

$$w[K_i'] = \begin{cases} 1/K_s & \text{if } |K_i'| < K_s/2 \\ 0 & \text{if } |K_i'| > K_s/2 \end{cases} \tag{12}$$

such that $K_s^2=C\sigma\gamma$, with $C=48\pi^2C'^2/(N\Delta V)$ being a discretization-specific constant. Since Kirchhoff's law has been proven analytically for a 1D uniform slab, we perform calibration runs on a uniform slab for both emission and absorption in order to obtain the calibration constant. We then use the same constant (which is discretization-specific) to convert emitted "flux" to emissivity for the case of the photonic crystal slab. Thus, we can calculate emissivity for a photonic crystal at *all* temperatures.

D. Limitations of the method

The approach we have outlined so far is able, as far as thermal fluctuations are concerned, to reproduce the wave nature of light, but not its particle nature.

From statistical mechanics [33], we know that the expected number of photons occupying a particular mode j is given by the Bose-Einstein distribution:

$$\langle n_j\rangle = \frac{1}{e^{\beta\epsilon_j}-1},$$

where $\langle n_j\rangle$ is the mean occupation number of state j, $\beta=1/kT$, where T is the temperature and k is Boltzmann's constant, and ϵ_j is the energy associated with the jth state.

The mean square deviation of the photon occupation number from this mean is given by [33]

$$\langle\Delta n_j^2\rangle = \frac{1}{\beta}\frac{\partial\langle n_j\rangle}{\partial\epsilon_j} = \langle n_j\rangle+\langle n_j\rangle^2. \tag{13}$$

Thus, we see that

$$\frac{\langle\Delta n_j^2\rangle}{\langle n_j\rangle^2} = 1+\frac{1}{\langle n_j\rangle}. \tag{14}$$

For a general particle in the Maxwell-Boltzmann limit, $-\mu/kT\gg 1$ and so the Bose-Einstein distribution can be approximated by $e^{\beta(\mu-\epsilon_j)}$. Plugging this into Eq. (13) gives

$$\frac{\langle\Delta n_j^2\rangle}{\langle n_j^2\rangle^2} = \frac{1}{\langle n_j\rangle}.$$

Therefore, we can think of the $1/\langle n_j\rangle$ term as arising from the particle nature of light (because in the Maxwell-Boltzmann limit, these photons do behave more like particles than waves). Consequently, by deduction, the 1 term in Eq. (14) accounts for the wave nature of light. This term dominates in the limit of $kT\gg\epsilon_j$.

Luo *et al.* [22] performed a statistical analysis on their ensemble data and found that $\sqrt{\langle\Delta I(\omega,T)^2\rangle}=\langle I(\omega,T)\rangle$. Thus, the stochastic electrodynamics that we have described so far reproduce the wave nature of light correctly. We can convert the fluctuations we see in our simulations to the real *physical* fluctuations by observing that $\langle\Delta n_j^2\rangle/\langle n_j\rangle^2=\exp(\hbar\omega/kT)$ for physical fluctuations, and then scaling the observed fluctuations by the factor $\exp(\hbar\omega/2kT)$. Therefore, $\sqrt{\langle\Delta I(\omega,T)^2\rangle}=\exp(\hbar\omega/2kT)\langle I(\omega,T)\rangle$.

III. DESCRIPTION OF NUMERICAL METHODS

Numerical simulations in our work are performed using a finite-difference time-domain (FDTD) algorithm [34]. These are exact (apart from discretization) 3D solutions of Maxwell's equations, including material dispersion and absorp-

tion. Equations (1) and (2) can be discretized in the standard way by writing $d^2\mathbf{P}(\mathbf{r},t)/dt^2 \approx [\mathbf{P}(\mathbf{r},t+\delta t)-2\mathbf{P}(\mathbf{r},t)+\mathbf{P}(\mathbf{r},t-\delta t)]/\delta t^2$ and $d\mathbf{P}(\mathbf{r},t)/dt \approx [\mathbf{P}(\mathbf{r},t+\delta t)-\mathbf{P}(\mathbf{r},t-\delta t)]/(2\delta t)$.

For 2D calculations, we choose a computational cell with dimensions $40\times2\times640$ grid points, corresponding to 40 grid points per lattice constant a. The faces of the cell normal to the x and y axes are chosen to have periodic boundary conditions, while the faces normal to the z axis (i.e., the top and bottom ones) have perfectly matched layers (PML) to prevent reflection. This is a 2D simulation of a 2D periodic system. The slab is placed in the middle of the cell, and flux planes are placed on either side of it at least $4a$ away. We run the simulation for a total of 81 600 time steps, chosen to give a frequency resolution of $0.001c/a$.

For 3D calculations, we choose a computational cell with dimensions $30\times30\times420$ grid points, corresponding to 30 grid points per lattice constant a. The faces of the cell normal to the x and y axes are chosen to have periodic boundary conditions, while the faces normal to the z axis (i.e., the top and bottom ones) have PML boundary conditions. The slab is placed one-third of the way down the cell, and flux planes are placed on either side of it at least $3a$ away. We run the simulation for a total of 60 000 time steps, also chosen to be sufficiently large to give a frequency resolution of $0.001c/a$.

For absorbance calculations, we illuminate the photonic crystal (PhC) slab with a normally incident, temporally Gaussian pulse. We record the fields going through flux planes on either side of the slab and perform a discrete Fourier transform on the time series of fields, which we use to calculate fluxes as functions of frequency $[\Phi(\omega)]$. We run the simulation once with the slab in place, and again with vacuum only. We record the fields going through flux planes on either side of the slab and perform a discrete Fourier transform on the time series of fields, which we use to calculate fluxes as functions of frequency, $\Phi(\omega)=\frac{1}{2}\mathrm{Re}\{\int\cdot\mathbf{E}^*(\mathbf{r},\omega)\cdot\mathbf{H}(\mathbf{r},\omega)\cdot d\mathbf{S}\}$. We run the simulation once with the slab in place, and again with vacuum only. To calculate reflectance, we know that $\mathbf{E}_{slab}=\mathbf{E}_{vac}+\mathbf{E}_{ref}$ is true above the slab (i.e., between the source and the slab), with $\mathbf{E}_{ref}$ being the field due to reflection. The reflectance is given by

$$R(\omega)\equiv\frac{\Phi_{ref}}{\Phi_{vac}}=\frac{-\frac{1}{2}\,\mathrm{Re}\left\{\int_{A_1}[\mathbf{E}_{slab}(\mathbf{r},\omega)-\mathbf{E}_{vac}(\mathbf{r},\omega)]^*\times[\mathbf{H}_{slab}(\mathbf{r},\omega)-\mathbf{H}_{vac}(\mathbf{r},\omega)]\cdot d\mathbf{S}\right\}}{\frac{1}{2}\,\mathrm{Re}\left\{\int_{A_1}\mathbf{E}^*_{vac}(\mathbf{r},\omega)\times\mathbf{H}_{vac}(\mathbf{r},\omega)\cdot d\mathbf{S}\right\}},$$

where A_1 is the flux plane corresponding to "1," and the minus sign in the numerator is there to make the reflected flux positive. This expression can be shown to simplify, in air, to $R(\omega)=[\Phi_1^{vac}(\omega)-\Phi_1^{slab}(\omega)]/\Phi_1^{vac}(\omega)$, where the flux plane closer to the light source is 1, and the flux plane further from the light source is 2. [One can show that the numerator becomes $\Phi_1^{vac}(\omega)-\Phi_1^{slab}(\omega)+\frac{1}{2}\mathrm{Re}\{\int_{A_1}(\mathbf{E}^*_{vac}\times\mathbf{H}_{ref}-\mathbf{H}_{vac}\times\mathbf{E}^*_{ref})\cdot d\mathbf{S}\}$ but the cross term vanishes for incoming and outgoing plane waves in vacuum, for which $\mathbf{E}$ and $\mathbf{H}$ are proportional.] Similarly, the transmittance is given by $T(\omega)=\Phi_2^{slab}(\omega)/\Phi_2^{vac}(\omega)$ and the absorbance is simply $A(\omega)=1-R(\omega)-T(\omega)$. This way, we obtain reflectance, transmittance, and absorbance spectra for PhC slabs.

We incorporate absorption into our simulations by means of the Drude model, according to the following equation:

$$\epsilon(\omega)=\epsilon_\infty+\frac{4\pi\sigma}{(\omega_0^2-\omega^2-i\gamma\omega)}, \tag{15}$$

where ϵ_∞, γ, ω_0, and σ are input parameters. In our case, we are concerned with metals, for which $\omega_0=0$.

For emittance calculations, we use the same setup except that we do not have a source plane. We include the random term ($\mathbf{K}$) in our updating of the polarization [see Eq. (2)], and we monitor the fluxes passing through the same two flux planes. We repeat this many times, and then perform an average of the fluxes. Averaging reduces the size of the fluctuations. The averaged fluxes are then multiplied by the same constant conversion factor that exists between the absorbance and the fluxes in the case of the 1D uniform slab, for which emittance and absorbance are known to be equal, analytically.

A note about time averaging and ensemble averaging is appropriate here. According to the ergodic theorem, time averages and ensemble averages are equivalent in the limit of long time and large ensemble. However, when a discrete Fourier transform (DFT) is involved, the situation is somewhat subtle. In the FDTD algorithm that we use, the simulation is run for a discrete number of time steps N, after which a DFT is taken over the time series of fields $\mathbf{E}(t)$ and $\mathbf{H}(t)$, producing fields as functions of frequency $\mathbf{E}(\omega)$ and $\mathbf{H}(\omega)$. The frequency resolution $(\Delta\omega)$ of the resulting DFT-produced spectrum is inversely proportional to the number of time steps for which the simulation is run: $\Delta\omega\sim1/N$. Thus, the net effect of increasing the length of the run is to increase the frequency resolution of the spectrum. However, the time series of fields (and therefore its true, continuous Fourier transform) follows a stochastic process, which consists, in general, of a background drift combined with random fluctuations [distributed according to the probability density function in Eq. (12)]. It is well known that stochastic pro-

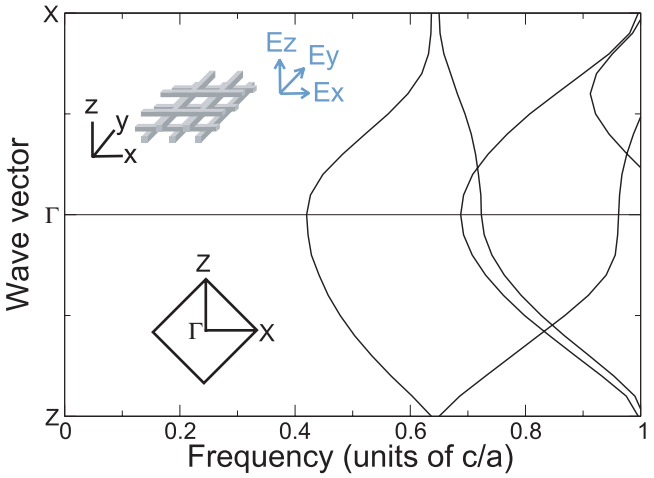

FIG. 1. (Color) Band structure for a 3D periodic woodpile structure made of perfect metal rods with a square cross section of width $0.25a$. We show bands along Γ-X and Γ-Z. The resolution is 30 grid points per a. We consider modes with all polarizations. We notice a large band gap in the system where light is forbidden from propagating, specifically from 0 to $0.42c/a$.

cesses, while continuous, are not differentiable anywhere, i.e., they are infinitely "wiggly." This means that as we increase N and thus frequency resolution, all we are doing is resolving the fluctuations at a finer and finer level of detail, i.e., increasing N does nothing to reduce the magnitude of the fluctuations. On the other hand, performing a larger number of such runs and then taking the ensemble average *does* reduce the magnitude of those fluctuations, and we get much better convergence. Therefore, it is only necessary to make N large enough to achieve a desired frequency resolution. Once that resolution is reached, computational power is better spent performing more ensemble runs. We see this quite clearly in Figs. 2 and 4, both of which are averaged over an ensemble of 40 runs. Runs in Fig. 2 are ten times as long as runs in Fig. 4. Note that the magnitudes of the fluctuations are comparable in the two figures, but the stochastic process is resolved at a much finer level of detail in Fig. 2, due to the higher frequency resolution that accompanies longer run times.

IV. 3D PERIODIC WOODPILE STRUCTURE

The first 3D periodic structure we consider is the woodpile [35]. Pioneering work on thermal emission and the nature of the band gap for this structure was done by Lin *et al.* [2–6,8]. We choose this particular structure because of the absence of linear bands at frequencies close to zero and the existence of a cutoff at $0.4c/a$ (there is a band gap in range $0–0.4c/a$). As a result, the structure behaves like a metal at low frequencies, with $\omega_p \approx 0.4c/a$.

The structure is made of metal rods with square cross sections of width $0.25a$ arranged so that the rods are orthogonal to each other in adjacent layers. These layers follow an *ABCD* pattern, such that *C* is the same as *A* shifted by half a lattice constant, and the same is true for *D* and *B* (*B* is the same as *A* rotated by 90°). It turns out that such a structure can be described by a body-centered cubic lattice whose basis consists of two rods, one on top of the other, forming a "plus" pattern. (One can also describe it as a stretched face-centered cubic lattice with a "cross" for a basis, but the ratio of the z length to the x or y length of the unit cell would be different, leading to an effectively orthorhombic lattice.)

In a general 3D periodic system, there are no mirror planes of symmetry that would allow us to separate the modes into TM and TE modes. This means that it is not possible, in general, to excite perpendicular and transverse polarizations separately; the different polarizations are coupled together. Therefore, it is necessary to use all three directions (x, y, and z) for polarizations in our simulations: all three must also be turned on for absorbance and for emittance calculations.

Figure 1 shows the band structure for a 3D periodic woodpile structure of perfect metal rods of width $0.25a$ and square cross section. We plot the bands from Γ-X and Γ-Z, since the Z direction is distinct from the X direction as a result of the basis of rods (though in the body-centered cubic *lattice*, they are equivalent directions). We see that there is a photonic band gap in the region $0–0.42c/a$. Above $0.42c/a$, there are bands which permit propagation of light through the photonic crystal. The upper limit of the band gap is determined by the frequency of the first band at Γ, since that is the frequency of the lowest energy propagating mode in this metallic woodpile system.

In Fig. 2, we see a comparison between emissivity and

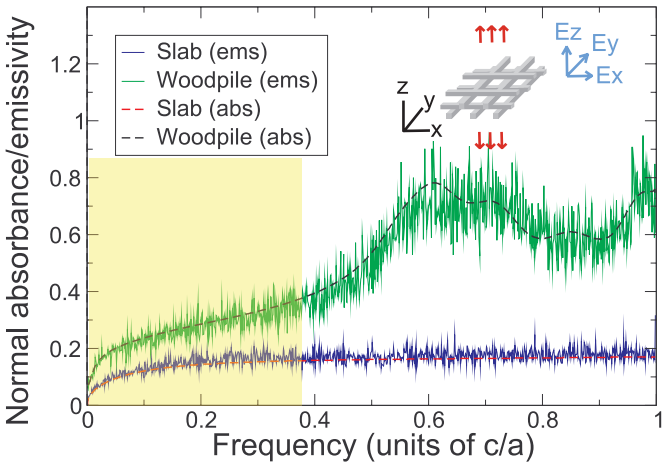

FIG. 2. (Color) Comparison between absorption and thermal emission (averaged over 40 runs) from a slab of 3D periodic woodpile made of metal rods, at normal incidence. We use a long computational cell with two unit cells of the woodpile structure in the z direction. For the metal, we use the Drude model with parameters $\epsilon_\infty = 1$, $\gamma = 0.3(2\pi c/a)$, $4\pi\sigma = 10(4\pi^2 c^2/a^2)$. The frequency resolution is $0.001c/a$. We see good agreement between the emissivity (green and blue solid lines) and the absorptivity (black and red dashed lines). We note also that the emission of the woodpile structure exceeds that of a uniform slab at all frequencies. The greatest enhancement comes from the nongapped region above $0.4c/a$, where the enhancement can be as high as a factor of 4. Translucent yellow shading indicates regions of pseudogap for such a woodpile slab structure made of imperfect metal rods, inferred from the absorption and/or emission spectrum.

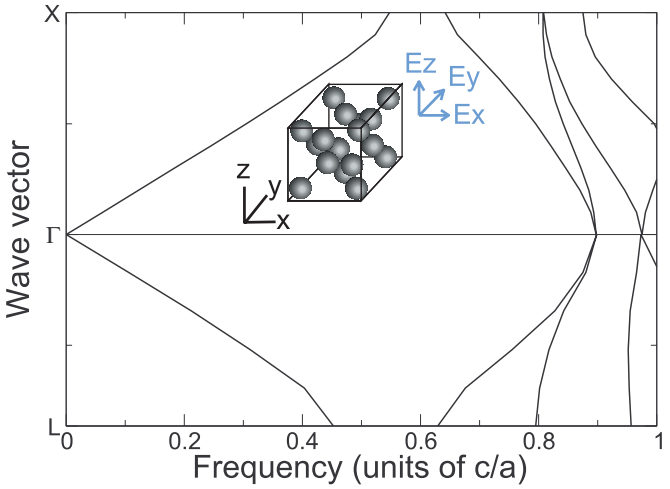

FIG. 3. (Color) Band structure for a 3D periodic metallodielectric structure made of perfect metal spheres of radius $0.177a$ in a background of Teflon (ϵ=2.1). We show bands along Γ-X and Γ-L. The resolution is 32 grid points per a. We consider modes with all polarizations. We note a complete band gap in the system where light is forbidden from propagating, specifically from $0.54c/a$ to $0.63c/a$.

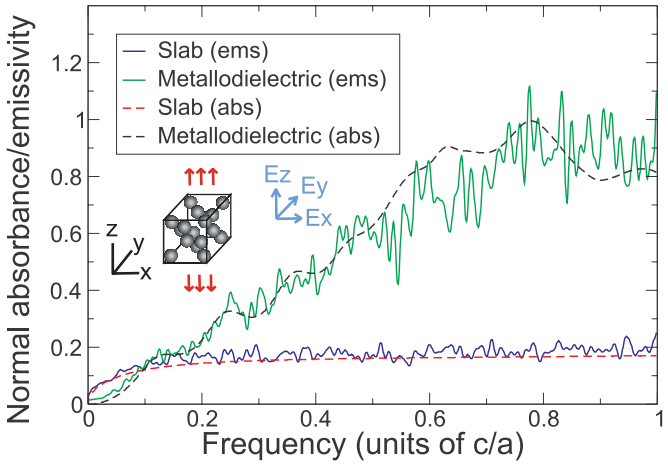

FIG. 4. (Color) Comparison between absorption and thermal emission (averaged over 40 runs) from a slab of 3D periodic metallodielectric structure made of metal spheres in a Teflon background, at normal incidence. We use a long computational cell with two unit cells of the metallodielectric structure in the z direction. For the metal, we used the Drude model with parameters $\epsilon_\infty=1$, $\gamma=0.3(2\pi c/a)$, $4\pi\sigma=10(4\pi^2c^2/a^2)$. Here, we use a lower frequency resolution of $0.01c/a$ in order to decrease the duration of each run. We see good agreement between the emissivity (green and blue solid lines) and the absorptivity (black and red dashed lines). We notice also that the emission of the metallodielectric structure exceeds that of a uniform slab at all frequencies above $0.1c/a$. The greatest enhancement comes from the nongapped region around $0.8c/a$, where the enhancement can be as high as a factor of 6. Note that the emissivity in that region is close to unity. Note also that the decreased run time leads to lower frequency resolution, as evidenced by the smoother spectrum. However, the size of the fluctuations remains unchanged (compare with Fig. 2), since is determined by the number of runs used in ensemble averaging.

absorptivity of the 3D periodic woodpile structure as a function of frequency. The jagged lines (green and blue) correspond to emissivity, while the dashed lines (black and red) correspond to absorptivity. We show absorptivity and emissivity spectra for both the woodpile and the uniform slab. The agreement is excellent. Furthermore, we note that the emissivity of the woodpile structure exceeds that of the uniform slab at all frequencies, but especially at frequencies above the photonic band gap of the system. (We indicate the pseudogap for the metallic woodpile slab with a translucent yellow color.)

These observations can be explained by considering the structure as being equivalent to a uniform metal slab, with a plasmon frequency ($\omega_p \equiv \sqrt{4\pi\sigma}$) equal to the upper bound of the band gap. In such a situation, we can derive expressions for the absorbance of the slab in two regimes: $\omega \ll \gamma \ll \omega_p$ and $\gamma \ll \omega \ll \omega_p$. This we do by calculating the reflectance using $R=[(n-1)^2+k^2]/[(n+1)^2+k^2]$, where n and k are the real and imaginary parts of the refractive index, defined by $\epsilon=(n+ik)^2$, and ϵ is the Drude dielectric function. Once we have the reflectance, we can obtain the absorbance by $A=1-R$. There is no transmission because the thickness of the slab is much greater than the penetration depth of the structure. If we perform this calculation for A in the low frequency regime, such that $\omega \ll \gamma \ll \omega_p$, we find that $A \approx \sqrt{8\omega\gamma/\omega_p}$. This explains the square-root dependence on frequency at extremely low frequencies. For the intermediate frequency regime, described by $\gamma \ll \omega \ll \omega_p$, we find that $A \approx 2\gamma/\omega_p$, which is independent of frequency. This explains the "plateau" region of the absorption spectrum, where frequency dependence is almost flat. Finally, we note that the effective penetration depth of the photonic crystal slab is larger than that of the uniform metal slab, because the photonic crystal contains both metal and air while the uniform slab contains only metal. A larger penetration depth corresponds to a smaller effective ω_p (since penetration depth goes as $1/\omega_p$). Therefore, we expect a larger absorbance for the photonic crystal slab than the uniform metal slab in both the low and intermediate frequency regimes, and this is indeed what we observe.

Above the band gap, the photonic crystal has bands which allow light to propagate through the bulk of the structure. Now, light emitted from deep inside the structure can escape and contribute to the emissivity of the crystal. This explains the significant enhancement of emission over that from a uniform slab at frequencies above that of the pseudogap region. The emissivity of a uniform slab is limited to contributions from within about one penetration depth of the surface of the metal; light emitted from the bulk cannot escape because there are no propagating modes available to transport the light to the surface. Emissive contributions from the bulk of the structure are the reason that the emissivity from the nongapped region of a photonic crystal slab is significantly higher than that from a uniform metal slab.

V. 3D PERIODIC METALLODIELECTRIC STRUCTURE

The next structure we consider is a 3D periodic metallodielectric structure made of metal spheres embedded in a

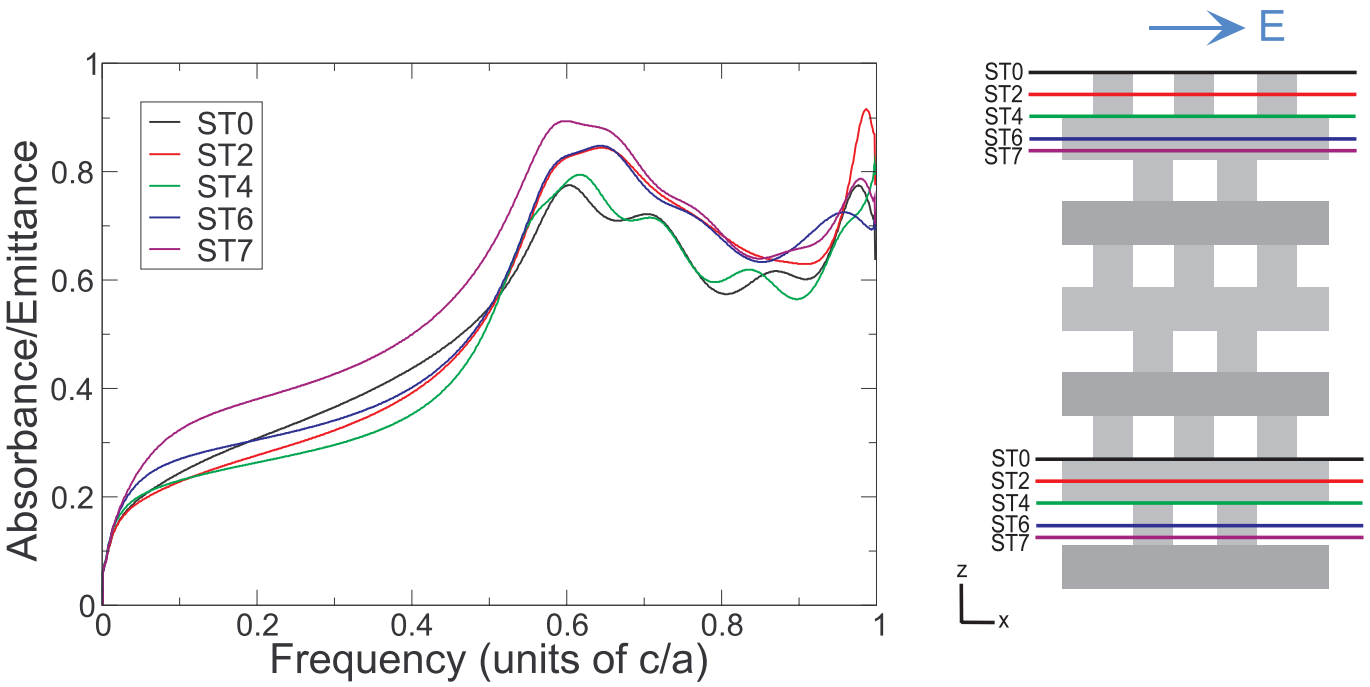

FIG. 5. (Color) Absorbance and/or emittance spectrum for a woodpile PhC slab made of imperfect metal rods for five different surface terminations. Light polarized along x is normally incident from the top of the cell. We use a long computational cell with two unit cells of the woodpile structure in the z direction. For the metal, we used the Drude model with parameters $\epsilon_\infty=1$, $\gamma=0.3(2\pi c/a)$, $4\pi\sigma=10(4\pi^2c^2/a^2)$. The inset is a schematic (lengths not to scale) indicating the surface terminations chosen. For all calculations, we keep the thickness of the slab to about two unit cells, so changing the surface termination amounts to shifting the structure within a two-unit-cell-thick slab "mask" which remains stationary as the structure is shifted, such that the total amount of material is kept constant. For instance, for ST0 the structure used is that between the two black lines, while for ST6, it is what lies between the two blue lines. ST7 appears to have the highest absorption and/or emission at all frequencies.

Teflon background ($\epsilon=2.1$), as studied by Fan, Villeneuve, and Joannopoulos [36]. In direct contrast to the woodpile structure investigated in the previous section, this metallodielectric structure *does* have linear bands at low frequencies. While the woodpile exhibited metallic behavior at low frequencies, here we expect to see uniform dielectric behavior in that same frequency range. Whereas the woodpile structure had a band gap from 0 to $0.42c/a$, the metallodielectric structure has propagating bands for all frequencies except for a small gap from $0.54c/a$ to $0.63c/a$. We will see dramatic differences between the emissivity of this structure and that of the woodpile.

The band structure of this metallodielectric structure is shown in Fig. 3. The metal spheres have radius $0.177a$ (where a is the lattice constant) and are arranged in a diamond structure. We show the bands from Γ-X and Γ-L, because the size of the band gap is determined by the frequencies of modes at these points in the Brillouin zone. The structure has a complete band gap between 0.54 and $0.63c/a$.

Figure 4 shows the results of comparing the absorptivity spectrum with the emissivity, calculated for a slab of the 3D periodic metallodielectric structure using stochastic electrodynamics. Once again, there is good agreement between emissivity and absorptivity. This time, we used a lower frequency resolution ($\Delta\omega=0.01c/a$) in order to reduce computation time. It is clear that the emission spectra are smoother here than in Fig. 2, but note that the size of the emissivity fluctuations (vertical fluctuations on the graph) are comparable to those in Fig. 2. This is because in both Figs. 2 and 4, the emissivity spectra were averaged over 40 runs, and, as we have already observed, the only way to reduce the size of the thermal fluctuations and increase convergence is to average over a larger ensemble of runs.

We note that for a large range of frequencies ($\sim 0.4-1.0c/a$) the emissivity of the photonic crystal far exceeds that of the uniform metal slab. This we already explained in the previous section in terms of emissive contributions from the bulk of the photonic crystal being allowed to escape because of the existence of propagating bands at those frequencies. The gapped region in this structure is so narrow ($0.54-0.63c/a$) that the dip in emissivity one would expect to see in that region is not noticeable. What is interesting is that for frequencies below $0.1c/a$, the emissivity of the photonic crystal is actually *lower* than that of the uniform slab. This requires some explanation.

At low frequencies, the photonic crystal behaves effectively like a uniform dielectric. We can see this from the band structure, which shows roughly linear bands in the region $0-0.4c/a$. Such uniform dielectric behavior can be modeled by the Drude dielectric function with an oscillator frequency that is much higher than the frequency regime we are interested in, i.e., we are working in the low-loss, dielectriclike regime given by $\omega \ll \gamma \ll \omega_0$. In this regime, the imaginary part of the dielectric function [see Eq. (6)], which is given by $\mathrm{Im}(\epsilon)=4\pi\sigma\gamma\omega/[(\omega_0^2-\omega^2)^2+\gamma^2\omega^2]$, is approximately linear in ω. The ac conductivity of the structure is

given by $\omega\epsilon_0 \mathrm{Im}(\epsilon)$, which goes as ω^2. Thus, the absorbance of the system, which is proportional to the integral of the ac conductivity over the volume of the structure, scales as ω^2 in the low frequency regime. This is precisely what we see in Fig. 4, and explains why the emissivity of the photonic crystal slab is lower than that for a uniform metal slab for $\omega \rightarrow 0$.

As Figs. 2 and 4 demonstrate, we have successfully verified Kirchhoff's law numerically for two very different 3D periodic photonic crystal structures.

VI. EFFECT OF SURFACE TERMINATION

One may wonder whether details of the absorption and emission spectra of a structure are affected by the surface termination one chooses. By surface termination, we refer to the plane in the periodic structure at which we terminate the PhC slab. Our choice of this termination may well have an effect on the surface modes that can be excited by incident light. The absorption-reflection-transmission caused by the bulk of the structure remain unchanged, because we keep the same thickness of the bulk structure in the PhC slab. We can imagine a window as wide as the thickness of the slab, moving downwards in the z direction across such a periodic structure of infinite extent; as the window moves, it reveals a slab of material with a different surface termination.

Figure 5 shows how absorbance and/or emittance of x-polarized light changes with surface termination in the case of the 3D periodic woodpile slab structure. We indicate in the inset the different ways in which the slab structure can be "terminated." The number following the letters "ST" indicate the position of the surface termination plane in relation to the structure. For example, ST2 is halfway down the first layer of blocks, and ST7 is three-quarters of the way down the second layer of blocks. It is remarkable how big a difference in absorption and/or emission can arise as a result of changing the surface termination. For example, ST7 seems to lead to the highest absorbance at all frequencies investigated, whereas ST4 has lower absorbance than almost all the other terminations.

In the band gap region $(0-0.4c/a)$, the light incident from the top of the cell is only able to penetrate the top surface; it is forbidden from propagating through the bulk of the crystal. Effectively, the incident light sees only the top surface, and any absorption and/or emission in the structure takes place near that surface. Thus, the absorption and/or emission spectra within the band gap are more sensitive to surface termination than that lying above the gap, for which absorption and emission are dominated by the bulk of the structure. This explains why the curves are more distinct in the band gap region than above it.

We notice also that above the band gap, the red and blue curves overlap significantly, as do the black and green curves. This requires some explanation.

We see from the schematic in Fig. 5 that the red and blue (ST2 and ST6) terminations are very similar, the only difference being that the blue structure is the same as the red structure rotated by 90° about the z axis. In fact, such a rotation maps the red onto the blue, and vice versa. In terms of surface terminations, they are the same: the termination that red has at the top of the slab is what blue has at the bottom, so that what the red structure emits from the top surface is what the blue structure emits from the bottom surface. Thus, we expect to see very similar absorbance and/or emittance spectra for the red and blue structures above the gap, and this is indeed what we see: the red and blue curves overlap significantly at frequencies above $0.5c/a$. The small differences comes from the fact that in the absorption calculation in Fig. 5, the light is incident from the top; this means that the top surface has a greater contribution to absorption than the bottom surface (even though both surfaces contribute because the bulk is transmitting above the gap), and causes the spectra to be polarization-sensitive, since the top surfaces of the red and blue structures are different.

At first glance, one may be tempted to think that the black and green (ST0 and ST4) terminations are related to each other in the same way. However, that is not the case: a 90° rotation will *not* map the black structure onto the green structure. Thus, as far as x-polarized light is concerned, they are irreducibly different surface terminations, in that one is orthogonal to the other. The curves show this clearly: the black and green curves are quite close together, but not as close together as the red and blue curves. And once again, the difference is most pronounced in the band gap region, where surface contributions dominate.

This information can be very useful in tailoring thermal emission properties of such woodpile slab structures, and more generally, photonic crystal slabs. By choosing a favorable surface termination, we can get over 20% enhancement in absorption and/or emission in certain frequency ranges over a randomly chosen surface termination.

VII. CONCLUSION

We outlined in detail the theory and implementation of stochastic electrodynamics following the Langevin approach and performed direct calculations of thermal emission for 3D periodic photonic crystal slabs via an FDTD algorithm. We demonstrated that emissivity and absorptivity are equal for a 3D periodic woodpile structure and a 3D periodic metallodielectric structure, by showing that such photonic crystal systems emit as much radiation as they absorb, for every frequency, up to statistical fluctuations. We also studied the effect of surface termination on absorption and emission spectra from these systems, and found that subtle changes in surface termination can have significant effects on emissivity. In terms of applications, the stochastic electrodynamic framework described in this work has many potential uses, including direct calculations of thermal emission in nonequilibrium systems, and systems with short thermalization times. One can also use this methodology to verify Kirchhoff's law numerically for finite-sized (nonslab) thermal objects. The results on surface termination can be used to enhance thermal emission for many such photonic crystal systems.

ACKNOWLEDGMENTS

We thank our colleagues Peter Bermel, Steven Johnson,

Elefterios Lidorikis, Chiyan Luo, and Alejandro Rodriguez for helpful discussions. This work was supported in part by the Croucher Foundation of Hong Kong and the MRSEC program of the NSF under Grant No. DMR-0213282.

[1] M. Planck, Ann. Phys. **4**, 553 (1901).
[2] S. Y. Lin *et al.*, Nature (London) **394**, 251 (1998).
[3] S.-Y. Lin, J. G. Fleming, E. Chow, J. Bur, K. K. Choi, and A. Goldberg, Phys. Rev. B **62**, R2243 (2000).
[4] J. G. Fleming, S. Y. Lin, I. El-Kady, R. Biswas, and K. M. Ho, Nature (London) **417**, 52 (2002).
[5] S. Y. Lin, J. Moreno, and J. G. Fleming, Appl. Phys. Lett. **83**, 380 (2003).
[6] S.-Y. Lin, J. G. Fleming, and I. El-Kady, Appl. Phys. Lett. **83**, 593 (2003).
[7] S.-Y. Lin, J. G. Fleming, and I. El-Kady, Opt. Lett. **28**, 1909 (2003).
[8] S.-Y. Lin, J. Moreno, and J. G. Fleming, Appl. Phys. Lett. **84**, 1999 (2004).
[9] D. L. C. Chan, E. Lidorikis, and J. D. Joannopoulos, Phys. Rev. E **71**, 056602 (2005).
[10] M. Florescu, H. Lee, A. J. Stimpson, and J. Dowling, Phys. Rev. A **72**, 033821 (2005).
[11] A. Mekis, A. Dodabalapur, R. E. Slusher, and J. D. Joannopoulos, Opt. Lett. **25**, 942 (2000).
[12] H. Sai, H. Yugami, Y. Akiyama, Y. Kanamori, and K. Hane, J. Opt. Soc. Am. A **18**, 1471 (2001).
[13] M. U. Pralle *et al.*, Appl. Phys. Lett. **81**, 4685 (2002).
[14] S. Enoch *et al.*, Appl. Phys. Lett. **86**, 261101 (2005).
[15] M. Laroche, R. Carminati, and J.-J. Greffet, Phys. Rev. Lett. **96**, 123903 (2006).
[16] S. Fan and J. D. Joannopoulos, Phys. Rev. B **65**, 235112 (2002).
[17] H. Sai, T. Kamikawa, Y. Kanmori, K. Hane, H. Yugami, and M. Yamaguchi, *Thermophotovoltaic Generation with Microstructured Tungsten Selective Emitters*, Proceedings of the Sixth NREL Conference on Thermophotovoltaic Generation of Electricity (AIP, Melville, NY, 2004), pp. 206–214.
[18] S. Peng and G. M. Morris, J. Opt. Soc. Am. A **13**, 993 (1996).
[19] A. R. Cowan, P. Paddon, V. Pacradouni, and J. F. Young, J. Opt. Soc. Am. A **18**, 1160 (2001).
[20] M. Meier, A. Mekis, A. Dodabalapur, A. Timko, R. E. Slusher, and J. Joannopoulos, Appl. Phys. Lett. **74**, 7 (1999).
[21] J.-J. Greffet and M. Nieto-Vesperinas, J. Opt. Soc. Am. A **15**, 2735 (1998).
[22] C. Luo, A. Narayanaswamy, G. Chen, and J. D. Joannopoulos, Phys. Rev. Lett. **93**, 213905 (2004).
[23] J.-J. Greffet, R. Carminati, K. Joulain, J. -P. Mulet, S. Mainguy, and Y. Chen, Nature (London) **416**, 61 (2002).
[24] M. Boroditsky, R. Vrijen, T. F. Krauss, R. Coccioli, R. Bhat, and E. Yablonovitch, J. Lightwave Technol. **17**, 1096 (1999).
[25] A. A. Erchak *et al.*, Appl. Phys. Lett. **78**, 563 (2001).
[26] M. Scalora, M. J. Bloemer, A. S. Pethel, J. P. Dowling, C. M. Bowden, and A. S. Manka, J. Appl. Phys. **83**, 2377 (1998).
[27] B. A. Munk, *Frequency Selective Surfaces Theory and Design* (Wiley, New York, 2000).
[28] A. Narayanaswamy and G. Chen, Phys. Rev. B **70**, 125101 (2004).
[29] B. J. Lee, C. J. Fu, and Z. M. Zhang, Appl. Phys. Lett. **87**, 071904 (2005).
[30] I. Celanovic, D. Perreault, and J. Kassakian, Phys. Rev. B **72**, 075127 (2005).
[31] C. M. Cornelius and J. P. Dowling, Phys. Rev. A **59**, 4736 (1999).
[32] S. M. Rytov, *Theory of Electric Fluctuations and Thermal Radiation* (Academy of Sciences Press, Moscow, Russia, 1953), English translation.
[33] F. Reif, *Fundamentals of Statistical and Thermal Physics* (McGraw-Hill, New York, 1965).
[34] A. Taflove and S. C. Hagness, *Computational Electrodynamics: The Finite-Difference Time-Domain Method* (Artech House, Norwood, MA, 2000).
[35] H. S. Sözüer and J. P. Dowling, J. Mod. Opt. **41**, 231 (1994).
[36] S. Fan, P. R. Villeneuve, and J. D. Joannopoulos, Phys. Rev. B **54**, 11245 (1996).